Energy & Environmental Science

ROYAL SOCIETY OF CHEMISTRY

PAPER

View Article Online
View Journal | View Issue

Cite this: *Energy Environ. Sci.*, 2025, **18**, 7514

Regulating segmental dynamics for ion clusters in polymer binders to realize high-areal-capacity electrodes in lithium batteries†

Dong-Yeob Han, ‡[a] Sungryong Kim,‡[b] Yeongseok Kim, [a] Haeryang Lim,[b] Gyeong Rok Lee,[d] Chi Keung Song,[e] Woo-Jin Song,[e] Hong Chul Moon, *[c] Soojin Park*[a] and Taiho Park *[b]

Received 31st March 2025,
Accepted 6th June 2025

DOI: 10.1039/d5ee01785h

rsc.li/ees

The growing demand for high-energy-density lithium batteries necessitates high-areal-capacity electrodes, typically involving high-mass-loading cathodes. However, achieving high mass-loading cathodes often leads to challenges such as structural instability and inefficient ion transport. In this study, a series of ionic soft polymer (ISP) binders have been designed to overcome these limitations. By modulating the segmental dynamics in the side chains, the ISP binder forms a reversible ion cluster, significantly enhancing ionic conductivity. Furthermore, electrostatic interactions and hydrogen bonding within the binder foster a robust network, providing strong adhesion and stability, while minimizing transition metal dissolution and surface side reactions. The ISP binder also exhibits remarkable self-healing properties and stretchability, effectively accommodating solvent-drying-induced stress. The designed binder-incorporated NCM811 cathodes achieve an impressive areal capacity of 17.9 mA h cm^{-2} at 86.1 mg cm^{-2} mass loading. A pouch-type Li metal full cell with a thin Li metal anode (40 μm) delivers a high energy density of 381.1 W h kg_{cell}^{-1}/1067.5 W h L_{cell}^{-1}, including packaging materials. This study demonstrates the promising potential of ISP binder to enable scalable high-areal-capacity electrodes for high-energy-density lithium batteries with enhanced stability and performance.

Broader context

The global shift toward renewable energy and electric mobility requires advanced lithium batteries with significantly high energy densities. Achieving this goal necessitates electrodes capable of supporting exceptionally high mass loadings of the active materials. However, the construction of these high-mass-loading electrodes poses significant challenges, including structural instability, slow ion transport, and rapid performance degradation, hindering their commercial viability. In this study, we address these critical limitations by engineering an innovative ionic soft polymer (ISP) binder. By precisely regulating the segmental dynamics of the polymer side chains, this binder facilitates the formation of reversible ion clusters, dramatically enhancing lithium-ion conductivity and electrode robustness. Moreover, the binder provides mechanical flexibility and self-healing capabilities, effectively preventing structural deterioration caused by drying-induced stresses and cycling fatigue. The resulting lithium battery electrodes achieve superior energy densities (381.1 W h kg_{cell}^{-1}/1067.5 W h L_{cell}^{-1} (including packaging materials)) and improved cycle life under practical conditions (N/P = 0.6 and E/C = 2.5 g A h^{-1}), demonstrating feasibility for scalable manufacturing. By overcoming key performance barriers, this approach supports the broader adoption of high-energy-density lithium batteries essential for accelerating global transitions toward sustainable energy storage and reducing the dependency on fossil fuels.

[a] *Department of Chemistry, Pohang University of Science and Technology (POSTECH), 77 Cheongam-Ro, Nam-gu, Pohang, Gyeongbuk, Republic of Korea. E-mail: soojin.park@postech.ac.kr*
[b] *Department of Chemical Engineering, Pohang University of Science and Technology (POSTECH), 77 Cheongam-Ro, Nam-gu, Pohang, Gyeongbuk, Republic of Korea. E-mail: taihopark@postech.ac.kr*
[c] *Department of Chemical & Biomolecular Engineering, Korea Advanced Institute of Science and Technology (KAIST), 291 Daehak-Ro, Daejeon, Republic of Korea. E-mail: hcmoon@kaist.ac.kr*
[d] *Department of Chemical Engineering, University of Seoul, 163, Dongdaemun-gu, Seoul, Republic of Korea*
[e] *Department of Chemical Engineering and Applied Chemistry, Chungnam National University, 99 Daehak-ro, Yuseong-gu, Daejeon, 34134, Republic of Korea*

† Electronic supplementary information (ESI) available. See DOI: https://doi.org/10.1039/d5ee01785h

‡ D. Y. H. and S. K. contributed equally to this work.

Introduction

The ever-growing demand for high-energy-density lithium (Li) batteries to power electric vehicles, portable electronics, and grid storage systems has driven relentless advancements in electrode materials and cell architectures.[1,2] Among these innovations, the development of high-areal-capacity electrodes has emerged as a critical strategy for enhancing energy density at the cell level.[3,4] The development of high-areal-capacity electrodes requires two key advancements in the design of high-mass-loading electrode architectures and the selection of cathode active materials with high specific capacities.[5,6] However, these advancements face significant challenges, particularly in retaining electrochemical performance, mechanical stability, and long-term cycling durability.[6,7]

High-mass-loading electrodes increase the active material content per unit area, reducing the proportion of inactive materials and ultimately improving the overall energy density.[8,9] However, fabricating ultrathick cathodes leads to significant mechanical and electrochemical challenges. An excessive electrode thickness exacerbates drying-induced capillary stresses, causing films to crack and delaminate beyond the "critical cracking thickness", which compromises the mechanical integrity and adhesion to the current collector, thereby degrading cell performance.[10,11] Moreover, the extended Li^+ diffusion path in thick electrodes results in uneven ion transport and sluggish through-thickness reaction kinetics, restricting active material utilization.[12,13] These challenges are further compounded by mechanical stresses during repeated cycling, promoting crack formation, delamination, and subsequent capacity fading. Various alternative fabrication methods and structural modifications have been explored to address these issues, including dry processing techniques and advanced electrode architectures. Dry processing mitigates solvent-induced capillary stresses but suffers from poor interparticle contact, weak mechanical cohesion, and limited adhesion to current collectors, resulting in suboptimal ionic and electronic conductivity.[14,15] Similarly, advanced architectures, such as ice templating, gel electrolyte-embedded systems, and three-dimensional (3D) printing can improve transport properties but typically require complex and expensive fabrication processes, limiting their scalability.[16–18]

Cathode active materials with high specific capacities, particularly, Ni-rich layered transition metal oxides (*e.g.*, $LiNi_{0.8}Co_{0.1}Mn_{0.1}O_2$, NCM811), also face severe stability challenges during cycling.[19] Highly reactive Ni^{4+} at high states of charge accelerates interfacial side reactions with liquid electrolytes, leading to electrolyte decomposition and the formation of a resistive, non-uniform cathode–electrolyte-interphase (CEI) layer.[20] Additionally, transition metal (TM) dissolution, particularly the reduction of Ni^{4+} to Ni^{2+}, results in TM deposition on the anode, increasing cell impedance and accelerating capacity decay.[21] Structural degradation further exacerbates these issues, as phase transitions from the layered structure to a rock-salt structure, driven by Ni^{4+} reduction and oxygen release, which blocks Li^+ transport and reduces reversible capacity.[20] Microcracks that develop during cycling expose fresh surfaces, even perpetuating interfacial degradation.

Polymer binders are crucial in stabilizing high-mass-loading cathodes by reinforcing structural integrity and mitigating interfacial side reactions.[22–24] Previously reported binders, primarily designed for interfacial stability, have demonstrated the ability to coat NCM811 particles uniformly and chelate dissolved TM *via* hydrogen bonding.[25–27] However, most reported polymer binders have overlooked critical properties such as stretchability, self-healing, and ionic conductivity, which are essential for stabilizing both the electrode surface and the inner cathode architecture. The absence of a stable 3D network and well-defined Li^+ transport pathways limits their effectiveness in ultra-thick electrodes, restricting their application in high-energy-density Li batteries.

Herein, we report the development of a series of ionic soft polymer (ISP) binders designed to address the critical limitations of conventional binder systems in high-mass-loading NCM811 cathodes. The binder is designed to regulate the segmental dynamics of side chains, which facilitates the formation of reversible electrostatic interactions within the polymer matrix. Increasing the density of ionic side chains systematically enhances the ionic conductivity of the ISP. Moreover, the incorporation of the reversible interactions and segmental mobility in the ISP binder enables it to effectively accommodate drying-induced stresses and mitigate cycling-induced degradation. Electrostatic interactions, coupled with hydrogen bonding, ensure uniform coverage of active materials with a stable CEI layer that suppresses undesired side reactions with liquid electrolytes, mitigating TM dissolution, phase transitions, and intergranular cracks. The synergistic effects of the ionic and mechanical properties of the ISP significantly enhance the electrochemical performance of NCM811 cathodes and enable the fabrication of high-areal-capacity electrodes (17.9 mA h cm^{-2} at a mass loading of 86.1 mg cm^{-2}) with uniform topologies, surpassing previously reported binder systems. Moreover, a pouch-type full cell incorporating the NCM811 cathodes and a thin Li metal anode (40 μm) achieves a remarkable energy density of 381.1 W h kg_{cell}^{-1}/1067.5 W h L_{cell}^{-1}, including packaging materials. This study explores the transformative potential of the ISP binder to pave the way for practical high-energy-density Li batteries using scalable manufacturing processes.

Results and discussion

The role of polymer binders in the cathode architecture is illustrated in Fig. 1a. The surfaces of the cathode particles and current collectors are primarily composed of metal oxides, necessitating hydrogen bond donor groups in the binder to ensure strong adhesion. However, the conventional polymer binder (polyvinylidene fluoride, PVDF) interacts with these surfaces only through van der Waals forces, leading to an inconsistent coating and poor structural integrity.[22] This non-uniform coating can destabilize the cathodes, particularly in high-mass-loading electrodes, resulting in crack formation (Fig. 1a inset). However, the ISP binder facilitated a uniform coating on the cathode materials owing to the hydrogen

bonding donor groups. Furthermore, the segmental dynamics and ion cluster of the ISP binder effectively stabilized the electrode structure even at high-mass-loading (Fig. 1a inset).[26] In addition, the ion cluster within the binder enhances Li^+ transport, mitigating ion transport limitations often associated with thick electrodes. To optimize the synergistic effects between the mechanochemical and ion conductive properties, lithium-3-sulfopropyl methacrylate (LSP) and methacryloyl 3,4-dihydroxyl-L-phenylalanine (DOPA) were randomly copolymerized in various ratios considering their reactivity, yielding a series of polymers: poly(LSP) (ISP100), poly($LSP_{0.67}$-*r*-$DOPA_{0.33}$) (ISP67), poly($LSP_{0.50}$-*r*-$DOPA_{0.50}$) (ISP50), poly($LSP_{0.33}$-*r*-$DOPA_{0.67}$) (ISP33), and poly(DOPA) (ISP0) (Note S1, ESI†). The chemical compositions and molecular weight distributions of the copolymers were characterised by nuclear magnetic resonance (NMR) spectroscopy and gel permeation chromatography (GPC) (Fig. S1 and S2, ESI†).

As the electrode fabrication process involves slurry casting in *N*-methyl-2-pyrrolidone (NMP), the solubility of the ISPs in NMP was assessed at a polymer concentration of 5 mg mL^{-1} (Fig. S3, ESI†). ISP100 exhibited poor solubility and formed precipitates, whereas the other ISPs were fully soluble. Therefore, further investigations were conducted using ISP0, ISP33, ISP50, and ISP67.

The incorporation of LSP with long alkyl side chains increases the free volume within the polymer matrix, as confirmed by differential scanning calorimetry (DSC). The series of ISPs, except for the ISP0, exhibited low glass transition temperatures (T_g) below 0 °C (Fig. S4, ESI†). In particular, ISP67 with the highest LSP content had the lowest T_g (−21 °C), indicating enhanced chain mobility. Moreover, the presence of sulfonate in LSP introduces reversible interactions between the polymers *via* electrostatic interactions (Fig. S5 and S6, ESI†). The large free volume and interaction in the polymer matrix allow for highly stretchable properties, which was confirmed by the tensile stress–strain (S–S) analysis of free-standing films (Fig. 1b). ISP0 with a relatively high T_g (13 °C) exhibited a 90.4% break of elongation, indicating rigidity. In contrast, ISP67 exhibited extremely high stretchability (817% break of elongation) compared to the other ISPs. However, its low Young's modulus indicates limited mechanical robustness, leading to reduced structural integrity. ISP33 and ISP50 exhibited 540% and 731% break of elongation, respectively, while maintaining a moderate Young's modulus.

To further investigate the interaction between the polymers, the rheological properties of the ISPs were analyzed (Fig. 1c). The storage modulus (G') represents the elastic properties, whereas the loss modulus (G'') indicates the viscous properties of the polymers. The frequency-dependent variation in the moduli classifies the polymer behavior into different mechanical states (Fig. S7a, ESI†). ISP0 and ISP33 exhibited higher G'' than G' at high angular frequencies (over 1 rad s^{-1}), transitioning from glassy to rubbery states at approximately 1 rad s^{-1} (Fig.

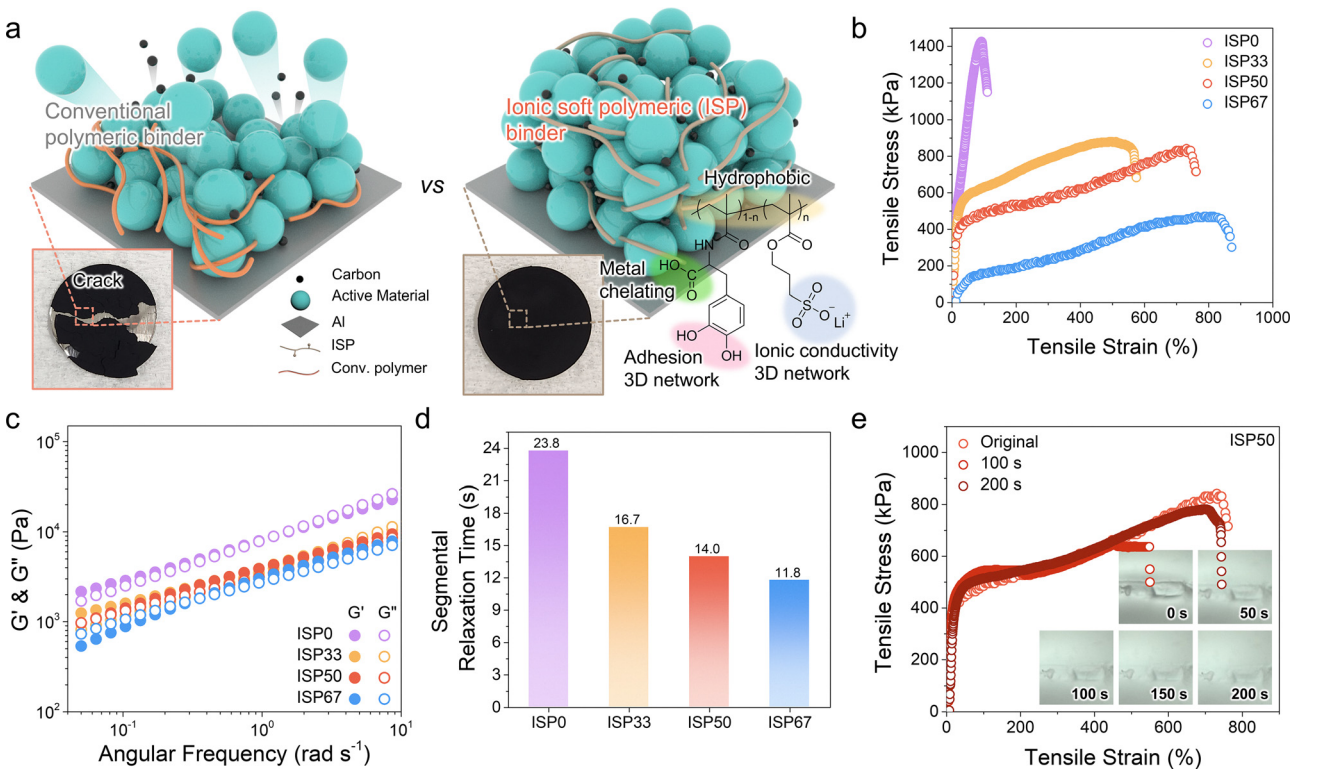

Fig. 1 (a) Illustration of a cathode based on conventional and ISP binders, along with the insets of the optical images of the cathode. (b) The tensile stress–strain (*S–S*) curves, (c) the storage (G') and loss (G'') moduli under angular frequencies, and the (d) segmental relaxation time (τ_s) at 0.05 rad s^{-1} of the ISPs. (e) The tensile *S–S* curves depending on the time (quantitative self-healing), along with insets of optical microscopy (OM) images (qualitative self-healing) of the ISP50.

S7b, ESI†). For ISP67, G' was higher than G'' at a high angular frequency (0.4–10 rad s^{-1}), indicating a predominantly elastic response. However, G' was significantly lower than G'' under a low angular frequency (0.05–0.4 rad s^{-1}), suggesting an alteration from the rubbery to the terminal region at 0.4 rad s^{-1}. In contrast, ISP50 exhibited consistently higher G' than G'' over the entire angular frequency region (0.05 to 10 rad s^{-1}), retaining a stable rubbery state (elastic properties).[28]

The segmental relaxation time (τ_s) of the polymer side chains was analyzed at 0.05 rad s^{-1} using eqn (1):[28,29]

$$J' = G' \Big/ ([\eta^*]\omega)^2 = \lambda/[\eta^*] \quad (1)$$

where J', G', $[\eta^*]$, ω, and λ are the storage compliance, storage modulus, complex viscosity, angular frequency, and relaxation time, respectively. The series of ISPs with more LSP showed shorter τ_s, indicating more vigorous segmental dynamics (Fig. 1d and Fig. S8, ESI†). This high segmental motion, coupled with reversible electrostatic and hydrogen bonding interactions, contributed to enhanced self-healing properties.[30] The self-healing ability was confirmed by qualitative analysis of optical microscopy (OM) image. The ISP0 film retained the cutting trace after 20 min, whereas the cutting traces in ISP50 and ISP67 disappeared within 200 s. Moreover, to quantitatively compare self-healing, S–S curves were obtained using the free-standing films (Fig. 1e and Fig. S9, ESI†). Similar to the OM images, ISP50 and ISP67 showed extremely fast self-healing (99.0 and 99.3%, respectively) after 200 s compared with the original films (Videos S1 and S2, ESI†).

As the ion moieties within the polymer increased, the formation of ion clusters became more facile (Fig. S5, ESI†). The results were similar to the increase in ionic conductivity (Fig. 2a).[31,32] ISP50 and ISP67 exhibited ionic conductivities of 1.19 and 0.89 mS cm^{-1}, respectively, outperforming PVDF (0.0011 mS cm^{-1}) (Fig. 2a and Fig. S10, ESI†). To further assess ion transport efficiency, temperature-dependent ionic conductivity was investigated to obtain the activation energy from the Vogel–Tammann–Fulcher plot (Fig. 2b).[33] The activation energy was also consistent with ion-cluster formation. Notably, ISP50 exhibited the lowest activation energy in the series of ISPs, confirming its high ionic transport properties. For more detail, the behavior of mobile ions within the polymer was analyzed *via* the relaxation frequency (Fig. 2c and d). The difference between charge (τ_c) and dielectric (τ_D) relaxation times indicates the time required for mobile ions to transport through the polymer matrix and reach the electrode interface.[34] It was difficult to accurately determine the charge relaxation frequency due to the high ionic conductivity of ISP50 and ISP67 at room temperature (Fig. S11, ESI†). Therefore, charge and dielectric relaxation frequencies were evaluated at −40 °C. ISP50 showed a shorter relaxation time difference (52 ms) than ISP67 (82 ms), indicating faster ionic mobility (Fig. 2d and Fig. S12, ESI†). Consequently, the formation of ion clusters contributed to the ionic conductivity; however, excessive ion-cluster formation was detrimental to ionic conductivity (Fig. 2e).[35]

In addition, the strain-dependent ionic conductivity of the ISPs was evaluated. When ISP0 was subjected to a 20% strain, the resistance increased 1.3 times compared to its initial state (Fig. S13a, ESI†). However, its ionic properties deteriorated under higher strain. ISP33, ISP50, and ISP67 exhibited minimal change in resistance at 20% strain compared to ISP0 and retained their ionic properties until 100% strain. Resistance

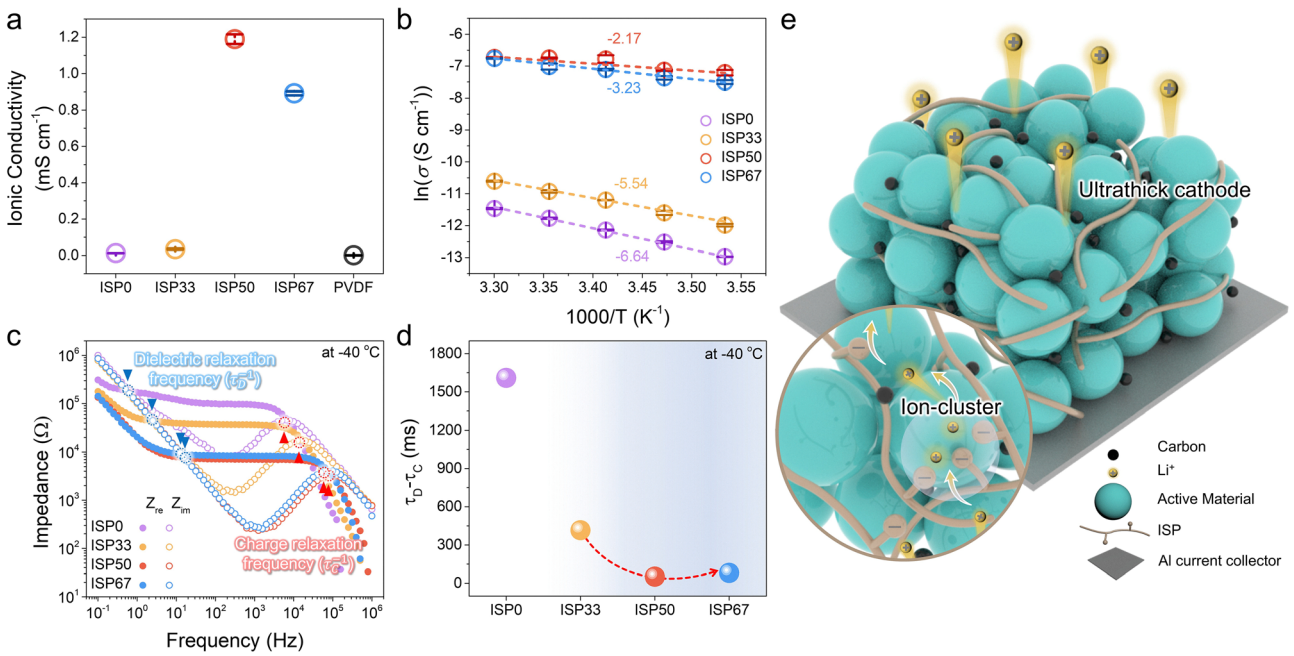

Fig. 2 (a) Ionic conductivity of the ISP series and PVDF. (b) Ionic conductivity depending on the temperature of the ISP series. (c) Real and imaginary impedance depending on the frequencies, and the (d) ion migration relaxation time of the ISP series at −40 °C. (e) Schematic diagram of ion clusters in the ultrathick cathode.

changes were examined across a range of 0–100% repeated strains for ISP33, ISP50, and ISP67. The ISPs exhibited a consistent variation in resistance under repeated strains (Fig. S13b, ESI†). Considering both mechanical and ionic properties, ISP50 demonstrated the most desirable characteristics for high-areal-capacity electrodes.

Leveraging the chemomechanical and ionic properties of ISP50, the binder was used to fabricate NCM811 cathodes. To evaluate the binder distribution and electrode homogeneity, analyses were conducted at the particle, micrometer, and millimeter scales. At the particle level, transmission electron microscopy (TEM) revealed a uniform and thin ISP50 binder layer (~4 nm) coating the NCM811 particles (Fig. 3a). The formation of ion clusters through the electrostatic interactions of LSP, combined with strong hydrogen bonding between the rich functional groups (*i.e.*, catechol, carboxyl, and amine groups) of DOPA and the oxygen-containing groups on NCM811, contributed to the even dispersion of the binder. These interactions promote tight adhesion and elastic adaptability, ensuring comprehensive particle coverage during slurry mixing and electrode processing. In contrast, the PVDF binders exhibited uneven and sporadic aggregation on the NCM811 surface because of their reliance on weak van der Waals interactions (Fig. 3d).

At the micrometer scale, scanning electron microscopy (SEM) images revealed that the NCM811 cathode with the ISP50 binder (denoted as the ISP50 cathode) displayed uniformly distributed particles throughout the entire electrode,

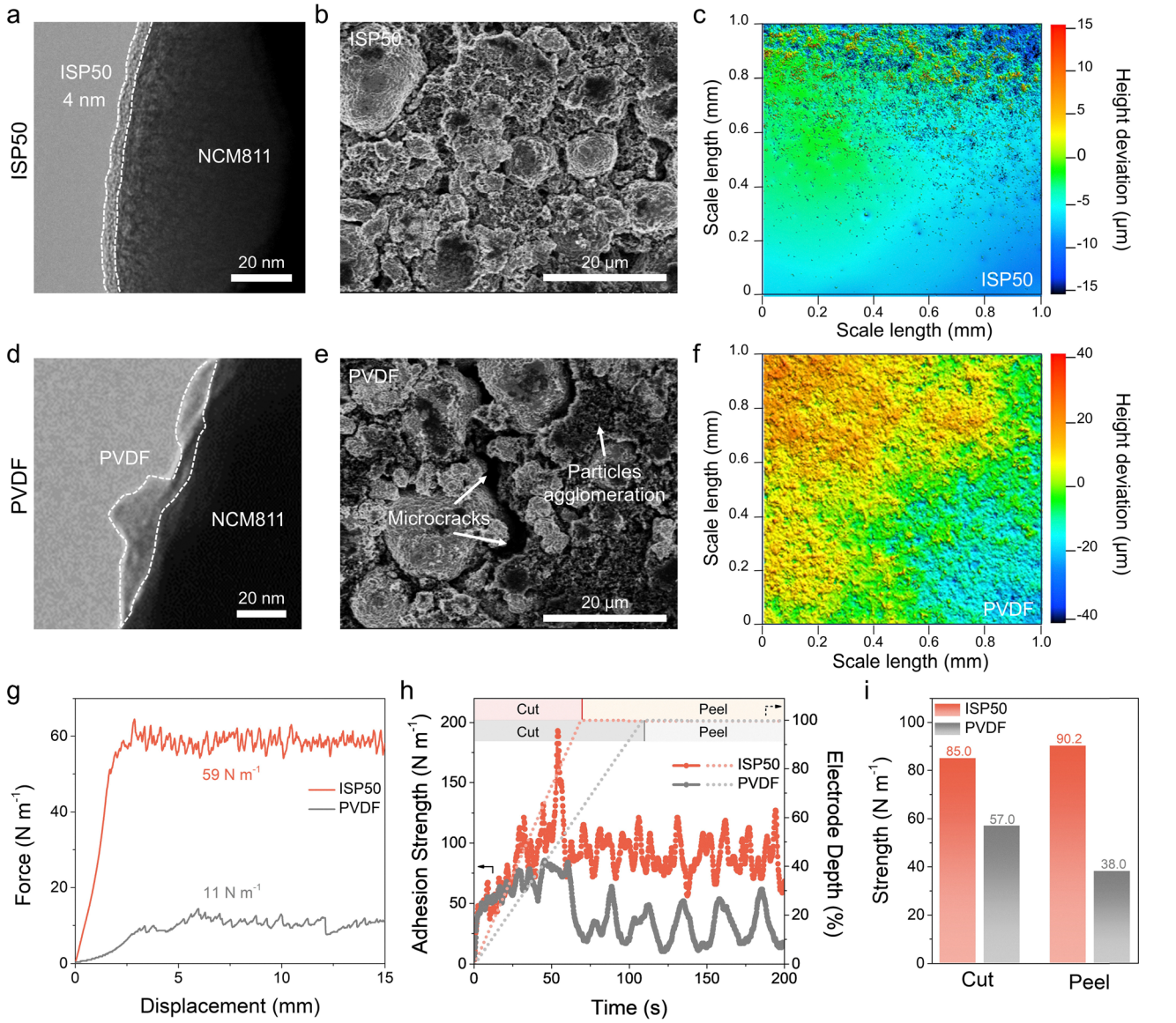

Fig. 3 Transmission electron microscopy (TEM) images of the (a) ISP50 and (d) PVDF binders on an NCM811 particle in the pristine state. Scanning electron microscopy (SEM) images of the (b) ISP50- and (e) PVDF-based NCM811 cathodes. 3D optical profiler images of the (c) ISP50- and (f) PVDF-based NCM811 cathodes. (g) 180° peeling test curves of the ISP50- and PVDF-based NCM811 cathodes. (h) The adhesive strength of the NCM811 cathodes at various electrode depths. (i) Adhesive strengths at the cut and peel modes of the NCM811 cathodes.

whereas the NCM811 cathode with the PVDF binder (denoted as the PVDF cathode) suffered from non-uniform particle distribution and agglomeration (Fig. 3b and e). The superior dispersion in the ISP50 cathodes, combined with the elasticity and self-healing properties arising from the ion cluster of the ISP50 binder, minimized microcrack formation caused by drying-induced stresses, whereas the PVDF cathodes exhibited noticeable microcracks, undermining mechanical stability. At the millimeter scale, 3D laser microscopy provided insights into the surface roughness of the electrodes. ISP50 cathodes displayed significantly lower height deviations across a 1.0 mm × 1.0 mm area, indicating a smoother and more uniform electrode surface compared to PVDF cathodes (Fig. 3c and f). This surface uniformity correlated with the superior dispersion properties of the ISP50 binder, further validating its ability to ensure electrode homogeneity.

The mechanical stability of the electrodes was assessed by a series of adhesion tests. The 180° peeling test using 3M tape showed that the ISP50 cathode exhibited an adhesion force more than five times higher than that of the PVDF cathode (59 N m^{-1} *vs.* 11 N m^{-1}) owing to the stronger secondary interactions with the current collector (Fig. 3g). In contrast, weak van der Waals interactions between PVDF and NCM811 led to inadequate particle adhesion and structural instability. Given that the 180° peeling test primarily represents the weakest interfacial adhesion site where mechanical cracks or

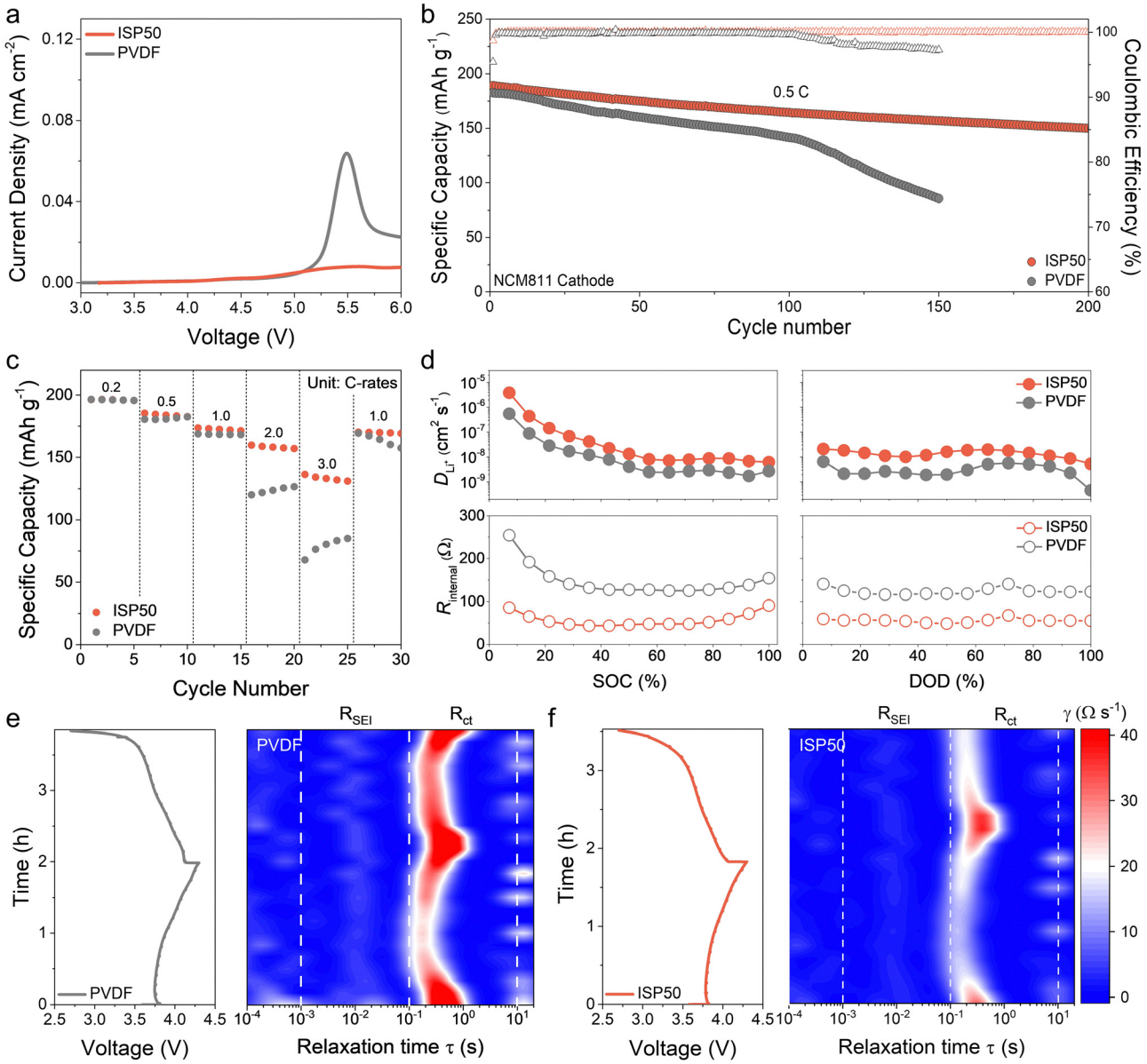

Fig. 4 (a) Linear sweep voltammetry (LSV) results from different binders. (b) Long-term cycling performance and (c) discharge rate capability NCM811 cathodes. (d) Internal resistance and Li^+ diffusion coefficient of the Li|NCM811 cells as a function of SOC and DOD. *In situ* DRT results of a Li||NCM811 cell with (e) PVDF and (f) ISP50 binders.

delamination occurred, the surface and interfacial cutting and analysis system (SAICAS) was employed to further assess both the cohesion strength within the cathode composite (cutting mode) and the adhesion strength to the current collector (peeling mode) (Fig. S14, ESI†).[36] During the cutting mode, which measures the cohesion strength within the cathode layer, both the PVDF and ISP50 cathodes initially exhibited similar adhesion near the surface. However, ISP50 cathodes demonstrated significantly higher cohesion strength deeper within the composite, averaging 85.0 N m^{-1}, compared to 57.0 N m^{-1} for PVDF cathodes (Fig. 3h and i). In the peeling mode, which evaluates adhesion strength to the current collector, ISP50 cathodes retained a stable and high adhesion strength of 90.2 N m^{-1}, whereas PVDF cathodes exhibited large fluctuations and a much lower average strength of 38.0 N m^{-1}. These findings confirm that ion-cluster formation and hydrogen bonding within ISP50 significantly enhance both the adhesion and cohesion properties, resulting in a structurally robust and homogeneous electrode architecture. In contrast, the inhomogeneous PVDF binder distribution and its reliance on weak van der Waals interactions compromise both adhesion and cohesion strengths, making it prone to delamination and mechanical failure. The synergistic effects of the electrostatic interactions and inter-binder cohesion in ISP50 ensure superior electrode integrity, making it an ideal binder for high-mass-loading cathodes in next-generation Li batteries.

The electrochemical stability of the ISP50 binder was evaluated using linear sweep voltammetry (LSV). Both the ISP50 and PVDF films exhibited minimal anodic currents below 4.5 V *vs.* Li/Li^+, with current densities remaining under 2.0 μA cm^{-2}, indicating negligible oxidative activity in this voltage range (Fig. 4a). Notably, the PVDF film showed a significant increase in oxidation current beyond 5.0 V, reaching approximately 63.0 μA cm^{-2} at 5.5 V. In contrast, the ISP50 film retained a much lower current density of about 7.8 μA cm^{-2} at 5.5 V, demonstrating its enhanced oxidative stability. Additionally, during the high-voltage floating test of the Li‖NCM811 cells, the ISP50 cathode consistently demonstrated smaller leakage currents across all voltages compared to the PVDF cathode, particularly at 4.8 V (Fig. S15, ESI†). These results confirm the high electrochemical oxidative stability of the ISP50 binder, which leads to the enhanced stability of NCM811 under high-voltage operation.

The electrochemical performance of NCM811 cathodes was evaluated using coin-type half cells with a high-areal-mass loading of 22.1 mg cm^{-2} (≈4.5 mA h cm^{-2}). The ISP50 cathode exhibited a slightly higher initial discharge capacity (208 mA h g^{-1}) and initial coulombic efficiency (92.2%) compared to the PVDF cathode (204 mA h g^{-1} and 90.4%). Additionally, the ISP50 cathode demonstrated a lower overpotential during the initial charge (3.82 V *vs.* 3.97 V for PVDF), which is attributed to the enhanced ionic conductivity and uniform particle dispersion provided by the ion cluster within the ISP50 binder (Fig. S16, ESI†).[37] The cycling performance of cathodes was evaluated at 0.5C/0.5C within a voltage window of 2.7–4.3 V. The ISP50 cathode demonstrated stable capacity retention of 80.1% after 200 cycles, whereas the PVDF cathode exhibited a gradual decline in capacity, retaining only 46.9% after 150 cycles (Fig. 4b). Furthermore, the discharge rate capabilities of the cathodes were evaluated by varying the discharge current from 0.2C to 3.0C under a constant charge current density of 0.2C (Fig. 4c). The ISP50 cathode exhibited superior rate performance across all rates, reflecting its facile redox kinetics owing to its ion cluster. To validate the optimality of the 50 : 50 composition, we conducted comparative electrochemical tests with ISP33, ISP50, and ISP67 binders (Fig. S17, ESI†). The ISP50 cathode retained 71.0% of its 0.2C capacity at 3.0C, outperforming ISP33 (57.3%) and ISP67 (47.6%), owing to its optimized ion cluster facilitating fast Li^+ transport. In long-term cycling at 0.5C, ISP50 retained 80.1% of its initial capacity after 200 cycles, compared to 64.4% (ISP33) and 69.0% (ISP67). These results, consistent with the polymer properties in Fig. 1 and 2, confirm ISP50 as the most effective binder composition.

The galvanostatic intermittent titration technique (GITT) was conducted after 30 cycles to further elucidate the Li^+ transport behavior (Fig S18, ESI†). The cell with the ISP50 cathode exhibited a lower internal resistance ($R_{internal}$) during charge and discharge processes, with an average value of 56.5 Ω compared to 135.0 Ω for the cell with the PVDF cathode (Fig. 4d). In addition, the ISP50 cathode achieved higher Li^+ diffusion coefficients (D_{Li^+}) over the entire state-of-charge (SOC) and depth-of-discharge (DOD) ranges. The average D_{Li^+} for the ISP50 cathode was 1.72×10^{-7} cm^2 s^{-1}, nearly an order of magnitude higher than that of the PVDF cathode (2.73×10^{-8} cm^2 s^{-1}), indicating the efficient Li^+ transport of the ISP50 binder.

The improved ion transport kinetics in the ISP50 cathode were also demonstrated by the distribution of relaxation time (DRT) analysis in the Li‖NCM811 cell. Herein, the charge transfer resistance (R_{ct}) at a low frequency ($10^1 < \tau < 10^{-1}$) corresponds to the faradaic processes through the electrode thickness, while the intermediate frequency peak ($10^{-1} < \tau < 10^{-3}$) represents the impedance of the SEI (R_{SEI}).[38] To visualize the energetic trends of R_{ct} and R_{SEI} during cycling, *in situ* electrochemical impedance spectroscopy (EIS)-combined with DRT mapping was performed on the Li‖NCM811 cell with different charge/discharge states (Fig. 4e and f). Compared with the PVDF cathode, the ISP50 cathode showed significantly lower R_{ct} values throughout the cycling. The appearance of resistance at a shorter relaxation time for the ISP50 cathode reflects faster Li^+ kinetics and more efficient electrochemical reactions. The ionic properties of the ISP50 cathode confirm that the ion cluster within the ISP50 binder provides highly conductive pathways for Li^+ transport and ensures strong interfacial contact between the active materials and the electrolyte. Furthermore, the synergistic effects of electrostatic interactions and hydrogen bonding reinforced both the structural and electrochemical stability of the ISP50 cathode, enhancing its performance in high-mass-loading electrodes.

To investigate the superior cycling performance of the ISP50 cathode, postmortem analysis of the electrodes was conducted after the cycling test. ICP-MS analysis revealed that the amounts of metallic Ni, Co, and Mn deposited on the Li metal

anode paired with the ISP50 cathode were significantly lower than those deposited on the Li metal anode with the PVDF cathode (Fig. S19, ESI†). This result was attributed to the chelating ability of the carboxylate and catechol groups in DOPA within the ISP50 cathode, as shown in Fig. 1a. These chelating groups trap TM ions, mitigating metal dissolution in accordance with Le Chatelier's principle.[39] Additionally, *ex situ* EIS analysis showed that the ISP50 cathode retained stable resistance over 100 cycles, while the PVDF cathode exhibited a significant increase in resistance after just 10 cycles, indicating accelerated interfacial degradation and poor cathode stability (Fig. S20, ESI†). Surface analysis of the cycled cathode using X-ray photoelectron spectroscopy (XPS) provided further insights into the superior interfacial properties of the ISP50 cathode. The C 1s spectra of the ISP50 cathode showed reduced C–O and C═O peaks compared to the PVDF cathode, indicating suppressed electrolyte decomposition due to the uniform coating provided by the ISP50 binder (Fig. 5a and b).[40] In the F 1s spectra, the PVDF cathode exhibited higher intensities of $Li_xPF_yO_z$ and LiF peaks, indicating more extensive reactions between the active material and acidic electrolyte species from the electrolyte along with $LiPF_6$ salt decomposition.[41] Furthermore, the O 1s spectra revealed a higher intensity of the TM–O peak for the PVDF cathode at 528.2 eV, highlighting greater surface exposure of NCM811 particles, which promotes side reactions. To further corroborate the composition and depth distribution of the cathode electrolyte interphase (CEI) layer, time-of-flight secondary-ion mass spectrometry (TOF-SIMS) analysis was applied to the cycled NCM811 cathodes. In TOF-SIMS 3D reconstruction images, the PVDF cathode displayed that Ni^- fragments were scarcely detected on the NCM811 surface, while high intensities of CEI components such as LiF_2^- and CP^- were observed (Fig. 5d). This accumulation of CEI species represents the formation of a thick uneven CEI layer from electrolyte decomposition, which hinders Li^+ kinetics and contributes to structural degradation. Conversely, the ISP50 cathode showed a thin, uniform CEI layer with a well-distributed Ni^- fragment signal and significantly lower CEI-related fragment intensities, ensuring efficient ion transport (Fig. 5c). To further confirm the suppression of parasitic reactions and phase transitions, gas evolution measurements were conducted using quadrupole mass spectrometry (QMS) following the formation cycle (Fig. S21, ESI†). The PVDF-based cell exhibited significantly higher concentrations of ethylene (from EC decomposition) and oxygen (from lattice oxygen release), whereas the ISP50-based cell showed markedly reduced evolution of these gases. This result directly demonstrates that the uniform and robust ISP50 binder coating effectively mitigates both electrolyte decomposition and oxygen release from the NCM811 lattice.

The structural stability of NCM811 cathodes with different binders was examined using synchrotron-based nano-computed-tomography (nano-CT) to visualize the morphological changes and internal particle cracks at high resolution. Nano-CT offers a distinct advantage over conventional imaging methods by enabling the investigation of interior particle cracks and subtle structural deformations that are not visible on the surface.[42,43] The 3D reconstructed image of the PVDF cathode revealed abnormal microcracks in the NCM811 particles (white arrows), whereas the ISP50 cathode retained a stable particle morphology and structural integrity (Fig. 5e and f). Similarly, *XY*-plane transmission X-ray microscopy (TXM) images showed extensive intergranular microcracks and pores in the PVDF cathode, whereas the ISP50 cathode exhibited no noticeable cracks. These results were corroborated by the cross-sectional SEM images, which revealed severe internal cracks in the PVDF cathode (Fig. S22, ESI†). The intergranular cracks in the PVDF cathode are attributed to the inhomogeneous lithiation and delithiation processes, leading to anisotropic volume changes and mechanical stress accumulation. This stress facilitates crack initiation and propagation, particularly along grain boundaries.[44,45] In contrast, the ISP50 binder provides uniform coverage and mechanical reinforcement, mitigating stress concentrations and preventing crack formation.

Furthermore, scanning transmission electron microscopy (STEM) with fast Fourier transform (FFT) and electron energy loss spectroscopy (EELS) analysis provided atomic-level evidence for the ability of the ISP50 binder to mitigate phase transformation. Notably, the thickening of the phase transformation layer to the rock-salt phase impedes Li^+ transport into the layered structure of the cathode and decreases the Li-storage capability of the cathode. The ISP50 binder drastically reduced the phase transformation thickness to 3.9 nm while retaining the layered structure at site B (Fig. 5g). In contrast, the PVDF cathode showed a significantly larger phase transformation region with a thickness of 19.3 nm (Fig. 5h). EELS analysis confirmed the interfacial stabilization by examining the oxidation states of the TMs (Fig. 5i and j). The energy loss difference (ΔE) in the O K-edge spectra, defined as the energy gap between the main-edge peak ($\approx$540 eV) and the pre-edge peak ($\approx$528 eV), revealed that the ISP50 cathode maintained higher ΔE values, indicating mitigation of the reduction of the Ni^{4+} to lower valence states (Ni^{2+} and Ni^{3+}) on the surface.[46,47] Additionally, a distinct O K pre-edge peak appeared at a relatively low depth for the NCM811 cathode cycled with the ISP50 binder, reflecting lower oxygen loss and a more stable cathode surface. Moreover, the Ni L_3/L_2 ratio declined more rapidly from the surface to the bulk in the ISP50 cathode, demonstrating its ability to suppress Ni^{2+} migration into the Li slabs, thereby causing rock-salt phase thickening and structural degradation. These results collectively demonstrate that the interfacial and structural stability of the ISP50 cathode arises from the synergistic effects of the electrostatic interactions by ion clusters, hydrogen bonding, and metal-chelating groups. These properties effectively suppress TM dissolution, minimize interfacial side reactions, and mitigate phase transitions, ensuring enhanced cycling performance and structural integrity of the NCM811 cathodes. The enhanced structural stability of the ISP50 cathode was further validated by differential capacity (dQ/dV) analyses, which corresponded to the cycle data presented in Fig. 4b (Fig. S23, ESI†). The dQ/dV curves of the ISP50 cathode exhibited minimal changes with no notable peak

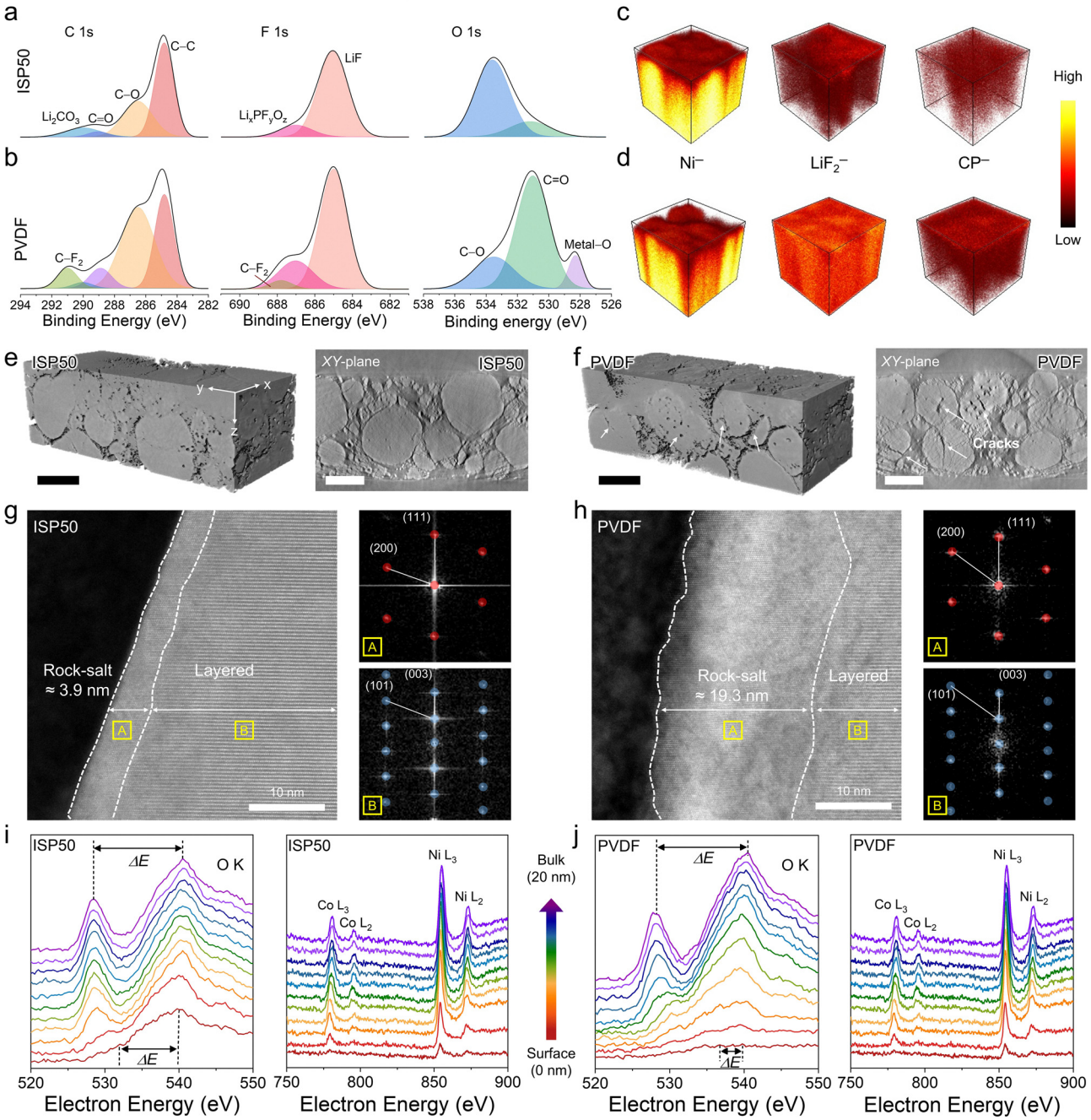

Fig. 5 C 1s, F 1s, and O 1s XPS spectra of (a) ISP50- and (b) PVDF-based NCM811 cathodes after 100 cycles. 3D visualization of several secondary-ion fragments on the cathode surface with (c) ISP50 and (d) PVDF binders. Synchrotron-based X-ray nano-tomography images of cycled NCM811 electrodes from (e) ISP50 and (f) PVDF binders (scale bar = 10 μm). STEM images with their FFT patterns for cycled NCM811 cathodes with (g) ISP50 and (h) PVDF binders. EELS plots in the range of 0–20 nm of cycled NCM811 cathodes for O K-, Co L_2, Co L_3, Ni L_3, and Ni L_2-edge spectra with (i) ISP50 and (j) PVDF binders.

shifts throughout the extended cycles, confirming its superior electrochemical reversibility and particle stability. Conversely, the PVDF cathode displayed pronounced peak shifts at around 4.2 V (H2-to-H3: hexagonal to hexagonal) and 3.7 V (H1-to-M: original hexagonal to monoclinic), reflecting significant polarization from impeded ion transport and structural deterioration.[48,49] To rigorously evaluate the interfacial robustness imparted by the ISP50 binder, cycling performance was examined under more aggressive conditions, including elevated voltages and high temperature (55 °C) operation (Fig. S24, ESI†). Although the PVDF cathode demonstrated relatively stable cycling at a cut-off voltage of 4.3 V, severe structural failures causing short circuits occurred at elevated voltages of 4.5 and 4.7 V within 90 and 60 cycles, respectively. These failures stemmed from exacerbated electrolyte decomposition, intensified intergranular cracking, and accelerated side

reactions under such harsh conditions.[25,50] Remarkably, the ISP50 cathode retained stable electrochemical cycling across the entire voltage range (4.3–4.7 V), owing to the robust three-dimensional polymer network, uniform binder coverage, and efficient suppression of electrolyte degradation and microstructural defects. These findings underscore the potential of the ISP50 binder for stabilizing high-energy-density Li battery cathodes under practical and demanding operating conditions.

To further demonstrate the practical applicability of the ISP50 cathodes for high-energy-density Li batteries, Li metal full cells were assembled by pairing ISP50 cathodes (22.1 mg cm^{-2} to 86.1 mg cm^{-2}) with a fixed Li metal anode (100 μm ≈ 20 mA h cm^{-2}), yielding a range of N/P ratios from 4.6 to 1.1. Owing to the superior ionic properties and structural/interface stability of ISP50, the Li metal full cells exhibited a proportional increase in the areal capacity, retaining stable voltage profiles across all loadings (Fig. 6a). Cross-sectional morphologies of the ISP50 cathodes with different mass loadings showed a uniform dispersion state, ensuring structural integrity even at an ultrahigh mass loading of 86.1 mg cm^{-2} with a thickness of 358 μm (Fig. S25, ESI†). Notably, the mass loading of 86.1 mg cm^{-2} (corresponding to 17.9 mA h cm^{-2}) enabled by the ISP50 far exceeded that of previously reported cathode binders (Fig. 6b). Additionally, the ISP50 cathodes retained the specific capacity of NCM811 even at an areal mass loading of 86.1 mg cm^{-2}, whereas PVDF cathodes exhibited severe cracking delamination, and a sharp capacity fade beyond 37.3 mg cm^{-2} (Fig. 6c). These results underscore the critical

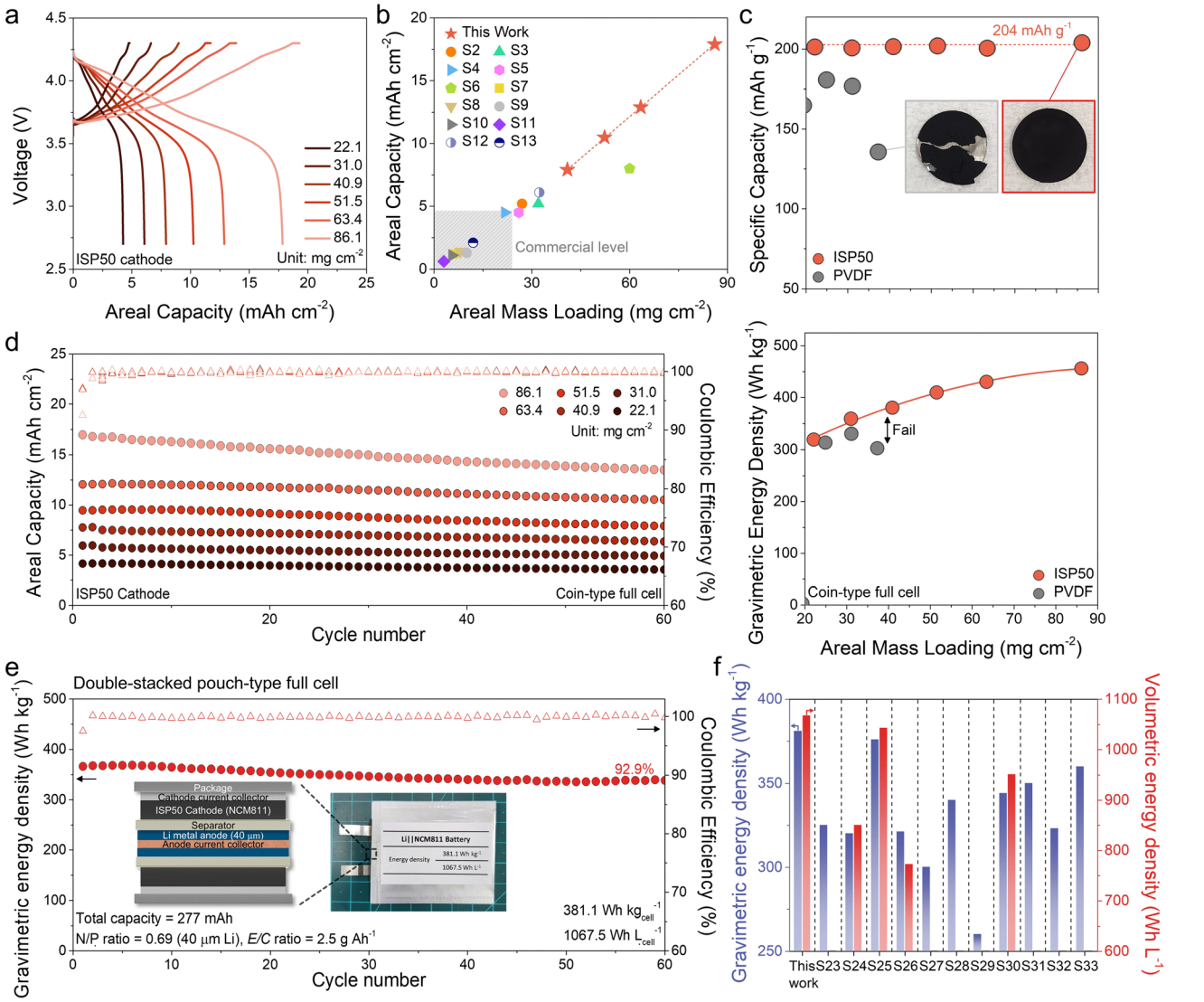

Fig. 6 (a) Galvanostatic charge/discharge profiles of the cells as a function of the areal capacity of the NCM811 cathodes with the ISP50 binder. (b) Comparison of the areal capacity (plotted as a function of areal mass loading) between the ISP50 cathode (this work) and previously reported cathodes containing various binders. (c) Specific gravimetric capacity (C/M_{NCM811}) and gravimetric energy density of the cells with different cathode binders. (d) Cycling performance of the ISP cathodes with different areal mass loadings (0.1C/0.1C for charge and discharge). (e) Cycling performance of the double-stacked pouch-type full cell with an N/P ratio of 0.69 (0.1C/0.1C for charge and discharge). (f) Comparison of the gravimetric and volumetric energy densities of the double-stacked pouch-type full cells fabricated in this work and previously reported high-energy-density pouch cells.

role of the ISP50 binder in maintaining cathode cohesion and electrochemical integrity under high-mass-loading conditions. While high-mass-loading electrodes are essential for achieving high-energy-density cells, prior studies have overlooked the importance of preserving the specific capacity at increasing loadings. The ISP50 cathode enabled a steady increase in the gravimetric energy density, reaching a plateau of 456.1 W h kg^{-1} at an areal mass loading of 86.1 mg cm^{-2} (calculation details in Table S1, ESI†). In contrast, PVDF cathodes suffered a gradual decline in energy density beyond 37.3 mg cm^{-2}, correlating with their compromised structural stability.

The cycling stability of the Li metal full cells at varying N/P ratios was evaluated at 0.1C/0.1C (Fig. 6d). Even at extremely high mass loadings, full cells with the ISP50 cathodes achieved 87.7% and 80.0% capacity retention for 63.4 mg cm^{-2} ($\approx$12.9 mA h cm^{-2}) and 86.1 mg cm^{-2} ($\approx$17.9 mA h cm^{-2}), respectively. In contrast, the PVDF cathode with a relatively low mass loading of 31.1 mg cm^{-2} displayed severe decay after 50 cycles (Fig. S26, ESI†). The stable capacity retention and electrochemical performance of the ISP50 cathode, even at low N/P ratios, were attributed to its ion-cluster facilitating efficient Li^+ transport, and its uniform coating on NCM811 particles, ensuring structural integrity through elastic and self-healing properties. Notably, the ISP50 cathodes above 40.0 mg cm^{-2} exhibited a sudden capacity drop around 80 cycles, rather than gradual fading (Fig. S27, ESI†). To investigate the origin of this failure, the ISP50 cathode with a mass loading of 40.9 mg cm^{-2} was recovered, rinsed, and reassembled in a fresh coin cell with new Li metal and electrolyte. The reassembled cell exhibited stable cycling performance over 90 additional cycles, confirming that the failure was primarily due to Li metal degradation or electrolyte depletion rather than cathode deterioration. To examine the practical limits of the ISP50 binder content, cathodes were fabricated with 2 wt% and 1 wt% binder. The maximum mass loading achievable without electrode cracking was 40.9 mg cm^{-2} for 2 wt% and 23.1 mg cm^{-2} for the 1 wt% binder (Fig. S28, ESI†). Despite the reduced binder content, both electrodes displayed stable voltage profiles and robust cycling performance at 0.2C, indicating that the electrochemical properties are retained. However, to fabricate ultrathick cathodes without cracking, 5 wt% ISP50 is preferable.

For commercial applicability, a double-stacked pouch-type full cell was fabricated, incorporating thick ISP cathodes (52.3 mg cm^{-2}) paired with a thin Li metal anode (40 μm, N/P ratio of 0.69) and a controlled E/C ratio of 2.5 g A h^{-1} (Fig. S29, ESI†). The fabricated pouch cell delivered a capacity of 277 mA h, achieving a remarkable energy density of 381.1 W h kg_{cell}^{-1}/1067.5 W h L_{cell}^{-1}, including packaging materials (Table S3, ESI†). This performance places it among the highest-reported energy densities for pouch-type full cells compared to the previously reported high-energy-density pouch-type full cells (Fig. 6f and Table S4, ESI†). The high-energy-density achieved in this configuration underscores the advantage of the ISP50 binders in enabling practical, high-mass-loading cathodes, particularly in Li-metal battery systems with stringent N/P and E/C ratios. Unlike many previously reported high-energy-density pouch cells, which require advanced electrolyte formulations optimized for Li metal anodes, the ISP50-based pouch cells achieved stable operation without electrolyte modifications. This highlights the intrinsic interfacial stability of the ISP50 binder and further reinforces its commercial potential. Moreover, the pouch cell retained 92.9% of its energy density after 60 cycles at 0.1C/0.1C (Fig. 6e). To determine whether the degradation of the pouch cell originated from the cathode or anode, the ISP50 cathode was recovered from the pouch cell after 60 cycles, rinsed, and reassembled in a coin cell with a fresh Li metal and electrolyte. The recovered cathode maintained stable cycling, confirming that the degradation stemmed from Li metal instability under lean-electrolyte (2.5 g A h^{-1}) and high-areal-capacity conditions ($\sim$10.5 mA h cm^{-2}) (Fig. S30, ESI†). This instability is attributed to the limited compatibility of the carbonate-based electrolyte, which fails to adequately suppress dendrite formation or parasitic reactions at the Li metal interface, leading to SEI thickening and electrolyte depletion. These findings underscore that while the ISP50 binder offers outstanding cathode stabilization, further improvements in long-term cycling performance will require integration with Li-stabilizing electrolytes to fully realize the commercial viability of high-energy-density Li metal pouch cells.

Conclusions

In this study, we introduced an ionic soft polymer (ISP) binder designed by regulating the segmental dynamics of polymer side chains to form ion clusters, enabling the fabrication of high-areal-capacity electrodes for Li batteries. The ion clusters enhanced Li^+ transport throughout the electrode and imparted self-healing capability and stretchability, effectively accommodating solvent-drying-induced stress. Furthermore, the ISP binder stabilized the Ni-rich layered cathodes by forming a uniform and adhesive protective coating with a stable CEI layer, which suppressed interfacial side reactions, mitigated phase transitions, and prevented intergranular cracking. This robust interfacial stabilization minimized transition metal dissolution, preserved the layered structure of NCM811 and ensured long-term electrochemical stability during cycling. Leveraging these ionic and mechanical properties, the ISP enabled the fabrication of high-mass-loading cathodes with an areal capacity of 17.9 mA h cm^{-2} at a mass loading of 86.1 mg cm^{-2}, substantially outperforming conventional binder systems. The practical feasibility of the ISP binder was further demonstrated in a double-stacked pouch-type Li metal full cell, which delivered an energy density of 381.1 W h kg_{cell}^{-1}/1067.5 W h L_{cell}^{-1} (including packaging materials) while retaining 92.9% energy retention over 60 cycles, even under stringent N/P (0.69) and E/C ratios (2.5 g A h^{-1}), without the need for advanced electrolyte formulations. These findings highlight the scalability and commercial viability of the ISP binder for fabricating high-areal-capacity electrodes, offering a practical pathway toward high-energy-density Li batteries with stable cathode architectures and extended cycle life.

Author contributions

D.-Y. H. and S. K. conceived the idea for the project. H. C. M., S. P., and T. P. supervised the research. D.-Y. H. investigated the electrode properties and electrochemical characterization. S. K. synthesized the polymers and analyzed polymer characterization. Y. K. analyzed the electrochemical properties. H. L. assisted with the NMR analysis. G. R. L. conducted the GPC analysis. W.-J. S. and C. K. S. conducted gas analyses. D.-Y. H., S. K., H. C. M., S. P., and T. P. wrote the manuscript.

Conflicts of interest

There are no conflicts to declare.

Data availability

The data supporting this article have been included as part of the ESI.†

Acknowledgements

This work was supported by the National Research Foundation of Korea (NRF) grant funded by the Ministry of Science and ICT (MSIT) (No. 2021R1A2C3004420, 2021R1A5A1084921, and RS-2024-00405905). Nano-CT was performed at the 7C beamline of the Pohang Accelerator Laboratory.

Notes and references

1 J. W. Choi and D. Aurbach, *Nat. Rev. Mater.*, 2016, **1**, 1.
2 R. Schmuch, R. Wagner, G. Hörpel, T. Placke and M. Winter, *Nat. Energy*, 2018, **3**, 267.
3 J.-H. Kim, N.-Y. Kim, Z. Ju, Y.-K. Hong, K.-D. Kang, J.-H. Pang, S.-J. Lee, S.-S. Chae, M.-S. Park, J.-Y. Kim, G. Yu and S.-Y. Lee, *Nat. Energy*, 2025, **10**, 295.
4 J. Wu, X. Zhang, Z. Ju, L. Wang, Z. Hui, K. Mayilvahanan, K. J. Takeuchi, A. C. Marschilok, A. C. West, E. S. Takeuchi and G. Yu, *Adv. Mater.*, 2021, **33**, 2101275.
5 Y. Kuang, C. Chen, D. Kirsch and L. Hu, *Adv. Energy Mater.*, 2019, **9**, 1901457.
6 Z. Du, D. L. Wood III, C. Daniel, S. Kalnaus and J. Li, *J. Appl. Electrochem.*, 2017, **47**, 405.
7 K.-Y. Park, J.-W. Park, W. M. Seong, K. Yoon, T.-H. Hwang, K.-H. Ko, J.-H. Han, Y. Jaedong and K. Kang, *J. Power Sources*, 2020, **468**, 228369.
8 S.-H. Park, P. J. King, R. Tian, C. S. Boland, J. Coelho, C. Zhang, P. McBean, N. McEvoy, M. P. Kremer, D. Daly, J. N. Coleman and V. Nicolosi, *Nat. Energy*, 2019, **4**, 560.
9 J.-H. Kim, K. M. Lee, J. W. Kim, S. H. Kweon, H.-S. Moon, T. Yim, S. K. Kwak and S.-Y. Lee, *Nat. Commun.*, 2023, **14**, 5721.
10 A. F. Routh, *Rep. Prog. Phys.*, 2013, **76**, 046603.
11 K. B. Singh and M. S. Tirumkudulu, *Phys. Rev. Lett.*, 2007, **98**, 218302.
12 J. Li, N. Sharma, Z. Jiang, Y. Yang, F. Monaco, Z. Xu, D. Hou, D. Ratner, P. Pianetta, P. Cloetens, F. Lin, K. Zhao and Y. Liu, *Science*, 2022, **376**, 517.
13 Z. Jiang, J. Li, Y. Yang, L. Mu, C. Wei, X. Yu, P. Pianetta, K. Zhao, P. Cloetens, F. Lin and Y. Liu, *Nat. Commun.*, 2020, **11**, 2310.
14 H. Oh, G.-S. Kim, J. Bang, S. Kim and K.-M. Jeong, *Energy Environ. Sci.*, 2025, **18**, 645.
15 M. Ryu, Y.-K. Hong, S.-Y. Lee and J. H. Park, *Nat. Commun.*, 2023, **14**, 1316.
16 J.-H. Kim, J.-M. Kim, S.-K. Cho, N.-Y. Kim and S.-Y. Lee, *Nat. Commun.*, 2022, **13**, 2541.
17 D.-Y. Han, H. B. Son, S. H. Han, C. K. Song, J. Jung, S. Lee, S. S. Choi, W.-J. Song and S. Park, *Small*, 2023, **19**, 2305416.
18 T.-S. Wei, B. Y. Ahn, J. Grotto and J. A. Lewis, *Adv. Mater.*, 2018, **30**, 1703027.
19 A. Manthiram, *Nat. Commun.*, 2020, **11**, 1550.
20 T. Li, X.-Z. Yuan, L. Zhang, D. Song, K. Shi and C. Bock, *Electrochem. Energy Rev.*, 2020, **3**, 43.
21 M. Jiang, D. L. Danilov, R.-A. Eichel and P. H. L. Notten, *Adv. Energy Mater.*, 2021, **11**, 2103005.
22 M. Lv, R. Zhao, Z. Hu, J. Yang, X. Han, Y. Wang, C. Wu and Y. Bai, *Energy Environ. Sci.*, 2024, **17**, 4871.
23 J. Kang, D.-Y. Han, S. Kim, J. Ryu and S. Park, *Adv. Mater.*, 2023, **35**, 2203194.
24 J. Kang, J. Y. Kwon, D.-Y. Han, S. Park and J. Ryu, *Appl. Phys. Rev.*, 2024, **11**, 011315.
25 H. Yang, R.-M. Gao, X.-D. Zhang, J.-Y. Liang, X.-H. Meng, Z.-Y. Lu and F.-F. Cao, *Adv. Mater.*, 2022, **34**, 2204835.
26 B. Chang, J. Kim, Y. Cho, I. Hwang, M. S. Jung, K. Char, K. T. Lee, K. J. Kim and J. W. Choi, *Adv. Energy Mater.*, 2020, **10**, 2001069.
27 N.-Y. Kim, J. Moon, M.-H. Ryou, S.-H. Kim, J.-H. Kim, J.-M. Kim, J. Bang and S.-Y. Lee, *Adv. Energy Mater.*, 2022, **12**, 2102109.
28 S. Kim, J. H. Kwon, Y. Bae, J. Kim, T. Park and H. C. Moon, *Energy Environ. Sci.*, 2024, **17**, 8102.
29 Y. Eom, S.-M. Kim, M. Lee, H. Jeon, J. Park, E. S. Lee, S. Y. Hwang, J. Park and D. X. Oh, *Nat. Commun.*, 2021, **12**, 621.
30 S. Kim, M. Ham, J. Lee, J. Kim, H. Lee and T. Park, *Adv. Funct. Mater.*, 2023, **32**, 2305499.
31 S. Kim, D.-Y. Han, G. Song, J. Lee, T. Park and S. Park, *Chem. Eng. J.*, 2023, **473**, 145441.
32 K. Dokko, D. Watanabe, Y. Ugata, M. L. Thomas, S. Tsuzuki, W. Shinoda, K. Hashimoto, K. Ueno, Y. Umebayashi and M. Watanabe, *J. Phys. Chem. B*, 2018, **122**(47), 10736.
33 K. M. Diederichsen, H. G. Buss and B. D. McCloskey, *Macromolecules*, 2017, **50**(10), 3831.
34 I. You, D. G. Mackanic, N. Matsuhisa, J. Kang, J. Kwon, L. Beker, J. Mun, W. Suh, T. Y. Kim, J. B.-H. Tok, Z. Bao and U. Jeong, *Science*, 2020, **370**, 961.
35 S. Jang, S. Y. Kim, H. Y. Jung and M. J. Park, *Macromolecules*, 2018, **51**(3), 1120.
36 B. Son, M.-H. Ryou, J. Choi, T. Lee, H. K. Yu, J. H. Kim and Y. M. Lee, *ACS Appl. Mater. Interfaces*, 2014, **6**(1), 526.

37 H.-J. Noh, S. Youn, C. S. Yoon and Y.-K. Sun, *J. Power Sources*, 2013, **133**, 121.
38 B. Ma, H. Zhang, R. Li, S. Zhang, L. Chen, T. Zhou, J. Wang, R. Zhang, S. Ding, X. Xiao, T. Deng, L. Chen and X. Fan, *Nat. Chem.*, 2024, **16**, 1427.
39 Y.-G. Cho, S.-H. Jung, S. H. Joo, Y. Jeon, M. Kim, K. M. Lee, S. Kim, J. M. Park, H. K. Noh, Y.-S. Kim, J.-E. Hong, S.-I. Jeon, T. Kim, S. K. Kwak, H. Kong and H.-K. Song, *J. Mater. Chem. A*, 2018, **6**, 22483.
40 J. Li and A. Manthiram, *Adv. Energy Mater.*, 2019, **9**, 1902731.
41 J. Ryu, D.-Y. Han, D. Hong and S. Park, *Energy Storage Mater.*, 2022, **45**, 941.
42 X. Lu, A. Bertei, D. P. Finegan, C. Tan, S. R. Daemi, J. S. Weaving, K. B. O'Regan, T. M. M. Heenan, G. Hinds, E. Kendrick, D. J. L. Brett and P. R. Shearing, *Nat. Commun.*, 2020, **11**, 2079.
43 J. Li, N. Sharma, Z. Jiang, Y. Yang, F. Monaco, Z. Xu, D. Hou, D. Ratner, P. Pianetta, P. Cloetens, F. Lin, K. Zhao and Y. Liu, *Science*, 2022, **376**, 6592.
44 B. Cui, Z. Xiao, S. Cui, S. Liu, X. Gao and G. Li, *Electrochem. Energy Rev.*, 2024, **7**, 27.
45 H. C. W. Parks, A. M. Boyce, A. Wade, T. M. M. Heenan, C. Tan, E. M. Pañeda, P. R. Shearing, D. J. L. Brett and R. Jervis, *J. Mater. Chem. A*, 2023, **11**, 21322.
46 B. Xu, C. R. Fell, M. Chi and Y. S. Meng, *Energy Environ. Sci.*, 2011, **4**, 2223.
47 H. Moon, H. Nam, M. P. Kim, S. M. Lee, H. Kim, M. H. Jeon, Y.-S. Lee, K. Kim, J.-H. Chun, S. K. Kwak, S. Y. Hong and N.-S. Choi, *Adv. Funct. Mater.*, 2023, **33**, 2303029.
48 Q. Gan, N. Qin, H. Guo, F. Zhang, H. Yuan, W. Luo, Z. Li, Y. Li, L. Lu, Z. Xu, L. Wang, J. Lu and Z. Lu, *ACS Energy Lett.*, 2024, **9**(4), 1562.
49 C. Xu, P. J. Reeves, Q. Jacquet and C. P. Grey, *Adv. Energy Mater.*, 2021, **11**, 2003404.
50 H. B. Son, S. Cho, K. Baek, J. Jung, S. Nam, D.-Y. Han, S. J. Kang, H. R. Moon and S. Park, *Adv. Funct. Mater.*, 2023, **33**, 2302563.

